



Spatial coherence from Nd^{3+} quantum emitters mediated by a plasmonic chain

JAVIER FERNÁNDEZ-MARTÍNEZ,^{1,4} SOL CARRETERO-PALACIOS,^{1,4} LAURA SÁNCHEZ-GARCÍA,¹ JORGE BRAVO-ABAD,² PABLO MOLINA,¹ NIELS VAN HOOFF,³  MARIOLA O. RAMÍREZ,¹  JAIME GÓMEZ RIVAS,³  AND LUISA E. BAUSÁ^{1,*} 

¹Dept. Física de Materiales, Instituto de Materiales Nicolás Cabrera and Condensed Matter Physics Center (IFIMAC), Universidad Autónoma de Madrid, 28049-Madrid, Spain

²Dept. Física Teórica de la Materia Condensada and Condensed Matter Physics Center (IFIMAC), Universidad Autónoma de Madrid, 28049 Madrid, Spain

³Dutch Institute for Fundamental Energy Research, DIFFER, and Eindhoven University of Technology, Groene Loper 5, 5612 AE Eindhoven, The Netherlands

⁴These authors contributed equally to this work

*luisa.bausa@uam.es

Abstract: Controlling the coherence properties of rare earth emitters in solid-state platforms in the absence of an optical cavity is highly desirable for quantum light-matter interfaces and photonic networks. Here, we demonstrate the possibility of generating directional and spatially coherent light from Nd^{3+} ions coupled to the longitudinal plasmonic mode of a chain of interacting Ag nanoparticles. The effect of the plasmonic chain on the Nd^{3+} emission is analyzed by Fourier microscopy. The results reveal the presence of an interference pattern in which the Nd^{3+} emission is enhanced at specific directions, as a distinctive signature of spatial coherence. Numerical simulations corroborate the need of near-field coherent coupling of the emitting ions with the plasmonic chain mode. The work provides fundamental insights for controlling the coherence properties of quantum emitters at room temperature and opens new avenues towards rare earth based nanoscale hybrid devices for quantum information or optical communication in nanocircuits.

© 2021 Optical Society of America under the terms of the [OSA Open Access Publishing Agreement](#)

1. Introduction

Optically active rare earth (RE) ions are currently the subject of intense research activity due to their wide-range applicability in a vast diversity of relevant technological fields. These systems play a key role in lasers, phosphors for solid-state lighting, or optical amplifiers in telecommunication systems [1–4]. In recent years, the areas of (bio)imaging, sensing or green energy have been strongly boosted by the incorporation of RE ions into different types of nanostructures [5–12]. Additionally, the present need of photon-matter interfaces for handling solid-state qubits, and the long coherent times of the nuclear spin transitions offered by RE ions, make RE doped crystals serious candidates as solid state platforms for quantum memories, which are essential components for the development of useful technologies in a future quantum global internet [13–17]. In this context, controlling the emission features of RE ions is crucial for most of the aforementioned applications and for the development of novel devices.

Recently, the association of plasmonic structures with RE doped crystals has been revealed as an interesting approach, offering robust solid-state platforms with emergent functionalities at subwavelength scales. Among others, plasmon-assisted RE based solid-state nanolasers operating at different spectral ranges [18–21] or dual wavelength operation produced by the simultaneous activation of an electronic- and a phonon-terminated transition enabled by plasmonic structures, have been recently demonstrated [22].

Here, we take a step further towards the manipulation at the nanoscale of coherent properties and angular control of the light emission of RE doped crystals by exploiting the coupling to plasmonic structures. By means of Fourier microscopy we demonstrate the presence of an interference pattern in the emission of Nd^{3+} ions located in the vicinities of a single plasmonic chain formed by closely-spaced Ag nanoparticles (NP), making evident a selective enhancement of the emitted light in specific directions. The results from numerical simulations verify a near-field coherent coupling of the Nd^{3+} emitters with the plasmonic mode supported by the NP chain, radiating light to the far field at specific directions. The plasmon induced coherence in the emission is evidenced by the interference pattern, which is qualitatively reproduced by the emission of multiple RE ions coupled to the same plasmonic mode in the NP chain.

The ability of surface plasmons to induce superradiance [23,24], spatial coherence and directionality of the emission has been predicted and observed [25–29]. In addition to the large spatial coherence observed in plasmon lasers [30], the transformation of the spontaneous emission into light with a high degree of partial spatial coherence [31], or the possibility of directional out-coupling of the emission of organic dye molecules through dipolar or multipolar plasmonic resonances [32] have been demonstrated. However, most of the studies on the modification of emission to create coherent light from the incoherent emission of many emitters involves excitons or organic molecules [33–35], and little work has been devoted to the use of plasmonic nanostructures to control the spatial coherence and directionality of the fluorescence of RE emitters in the absence of a photonic cavity [36]. Our results open new avenues for the manipulation of RE emission and the potential use of plasmon mediated ion-ion interaction processes to control the spatial coherence between quantum emitters at room temperature, which could be of interest for the development of novel solid state platforms for imaging, quantum technologies or sensing applications.

2. Results and discussion

The system under study is described in Fig. 1(a). It consists of a ferroelectric LiNbO_3 crystal doped with optically active Nd^{3+} ions ($\text{Nd}^{3+}:\text{LiNbO}_3$) on which millimeter length chains of Ag NPs have been formed on the ferroelectric domain boundary surfaces of the crystal by a photochemical method. The average size of the Ag NPs forming the plasmonic chain is around 50 nm and the separation distance between consecutive NPs close to 2 nm [37]. Nd^{3+} ions substitute for Li^+ cations and are homogeneously distributed into the LiNbO_3 crystal [38]. The relatively low Nd^{3+} concentration ($5.4 \times 10^{19} \text{ cm}^{-3}$) allows to disregard the presence of Nd^{3+} pairs in the crystal and the ion-ion interactions.

For the experiments, a 100x microscope objective (N.A.=0.9) was used to focus the excitation beam (tuned at 590 nm) onto a region of the $\text{Nd}^{3+}:\text{LiNbO}_3$ crystal surface containing a single plasmonic chain. The area of the excited crystal surface was around $5 \mu\text{m}^2$ (dashed circle on the micrography of Fig. 1(a)). The fluorescence emitted from Nd^{3+} ions was collected in backscattering configuration with the same microscope objective. A simplified energy level scheme of Nd^{3+} ions is shown in Fig. 1(b). It displays the inter-configurational $4f-4f$ optical transitions of Nd^{3+} ions relevant to this work, i.e., absorption at the $^4\text{I}_{9/2} \rightarrow ^4\text{G}_{5/2} + ^2\text{G}_{7/2}$ transition (green arrow indicates the excitation wavelength at 590 nm) and the $^4\text{F}_{3/2} \rightarrow ^4\text{I}_{9/2}$ and $^4\text{F}_{3/2} \rightarrow ^4\text{I}_{11/2}$ emission transitions centered at around 900 nm and 1080 nm, respectively (red arrows). The grey arrow represents the non-radiative decay from the optically excited state to the $^4\text{F}_{3/2}$ metastable state from which emission occurs. Figure 1(c) shows the numerically calculated scattering spectrum of the Ag NP chain (blue line) for a plane wave polarized along the chain axis. The spectrum has been calculated by solving the Maxwell's equations with the use of the boundary-element method (BEM) [39]. It shows an intense and spectrally broad longitudinal mode centered at around $\lambda \approx 600 \text{ nm}$ with a strong radiative character that mainly arises from the dipole-dipole coupling of the Ag NPs forming the chain [40]. This plasmonic mode has

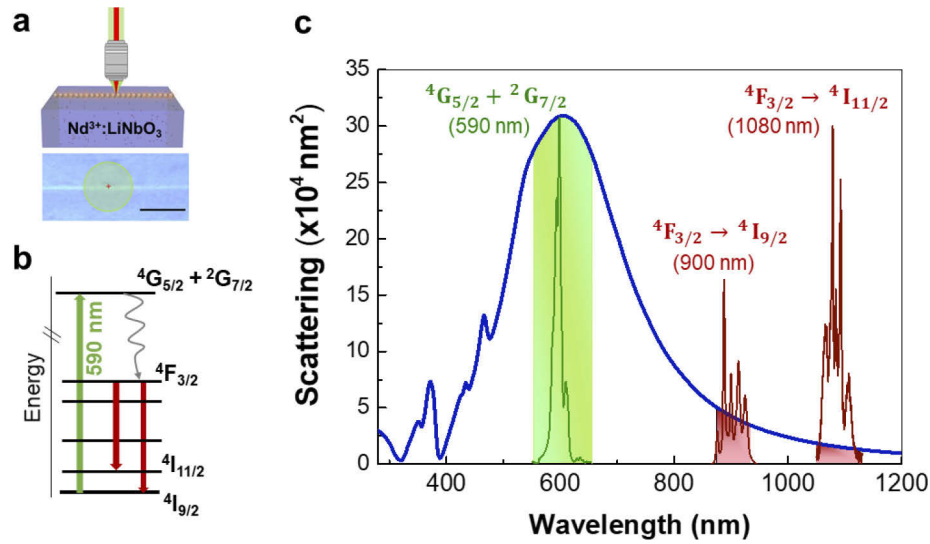


Fig. 1. (a) Top: Schematics of the hybrid plasmonic solid state system. Bottom: optical micrograph of the crystal surface showing the plasmonic chain and the excitation area; the scale bar corresponds to 2 μm . (b) Simplified energy level scheme of Nd^{3+} ion displaying the relevant electronic transitions employed in this work. The Nd^{3+} excitation at 590 nm (green arrow) and emission transitions centered at 900 and 1080 nm (red arrows) are indicated. (c) Calculated scattering spectrum of a Ag NP chain for light polarized along the chain axis (blue line) together with the normalized experimental absorption (green) and emission spectra (red) of Nd^{3+} ions in LiNbO_3 .

been shown to be useful to enhance a variety of optical processes such as Nd^{3+} absorption, photoluminescence (PL) or lasing at the nanoscale, since it extends from the VIS to the NIR, overlapping the spectral region of the most important absorption and emission transitions of Nd^{3+} [37,41]. For illustrative purposes, the Nd^{3+} absorption band used for the excitation and the emission spectra associated with the $^4\text{F}_{3/2} \rightarrow ^4\text{I}_{9/2}$ and $^4\text{F}_{3/2} \rightarrow ^4\text{I}_{11/2}$ transitions of Nd^{3+} have been included in Fig. 1(c). These spectra show a clear structure, which result from the Stark splitting of the involved $^4\text{F}_{3/2}$, $^4\text{I}_{9/2}$ and $^4\text{I}_{11/2}$ manifolds due to the effect of the host crystal field. At this point, it should be mentioned that previous studies have revealed the forced electric-dipole character of the optical transitions of Nd^{3+} ion in the LiNbO_3 matrix [42]. Such electric-dipole character will allow us to depict the Nd^{3+} emitters as single electric-dipole sources when analyzing the interaction between Nd^{3+} ions and the plasmonic mode supported by the linear chain in the near-field.

The effect of the plasmonic chain on the coherence properties and on the angular distribution of the far field pattern emitted by Nd^{3+} doped LiNbO_3 was analyzed by Fourier microscopy. Figure 2(a) shows a schematic of the experimental setup (see Methods). The study was carried out in two spectral regions by collecting separately the emission from the $^4\text{F}_{3/2} \rightarrow ^4\text{I}_{9/2}$ and from the $^4\text{F}_{3/2} \rightarrow ^4\text{I}_{11/2}$ optical transitions of Nd^{3+} ions. It is important to mention that no emission was detected outside these spectral regions. Figure 2(b) shows two optical micrographs corresponding to the Fourier images of Nd^{3+} emission at 900 nm ($^4\text{F}_{3/2} \rightarrow ^4\text{I}_{9/2}$ transition) obtained from the same sample in the proximities of the plasmonic chain and in a bare region without chain. The presence of an interference fringe pattern is only detected when the emission is collected around the plasmonic chain. Figure 2(c) displays the intensity distribution in the k -space obtained after subtracting the Fourier images in Fig. 2(b). In this manner, the effect of the Ag NP chain on the Nd^{3+} ions can be isolated from the background emission from the rest of

Nd^{3+} ions, which are also excited by the laser beam. The normalized cross-section profile along k_x at $k_y = 0$ is shown in Fig. 2(d). The effect of the metallic chain on the emission of Nd^{3+} ions is clearly seen. The Fourier image plane reveals the formation of an interference pattern, which indicates the possibility that the plasmonic chain imposes spatial coherence to the emission of Nd^{3+} ions located in its proximity.

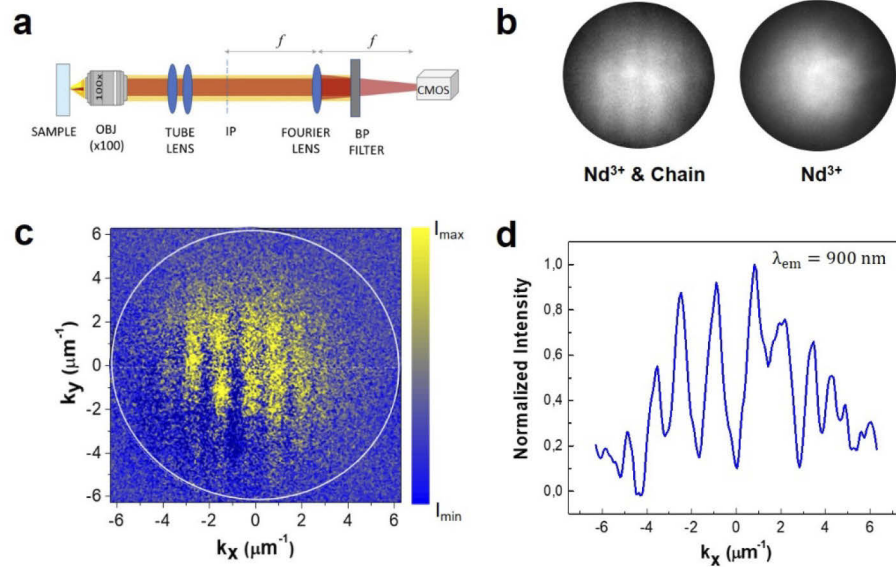


Fig. 2. (a) Schematics of the experimental setup used to collect and analyze the angular distribution of the Nd^{3+} emission from the sample. (b) Optical micrographs corresponding to the Fourier images recorded at 900 nm ($^4\text{F}_{3/2} \rightarrow ^4\text{I}_{9/2}$ Nd^{3+} transition) obtained in the proximities of the plasmonic chain (left) and in a region without chain (right). (c) Fourier image of the Nd^{3+} emission (900 nm) obtained by subtracting the images in b). The outermost circle indicates the maximum angular collection range provided by the objective. (d) Normalized cross-sectional profile along k_x at $k_y = 0$.

As observed from the interference patterns, the metallic chain produces a strong modification of the angular distribution of the Nd^{3+} emission. Figure 3(a) shows the interference pattern together with the corresponding angular distributions of the radiated emission at 900 nm ($^4\text{F}_{3/2} \rightarrow ^4\text{I}_{9/2}$) in the presence of the plasmonic chain. Well-resolved lobes (with angular separation of around 14° between the most intense maxima) can be distinguished when the excitation beam is focused at the immediacy of the metallic chain. The presence of emission directionality is also observed in the spectral region corresponding to the $^4\text{F}_{3/2} \rightarrow ^4\text{I}_{11/2}$ transition of Nd^{3+} ions at 1080 nm. The corresponding fringes pattern and the angular distribution for this emission wavelength are shown in Fig. 3(b). As expected, the separation between maxima is slightly larger than that observed for the emission at 900 nm, the angular separation between the most intense lobes being around 18° . A sketch of the effect of the metallic chain on the Nd^{3+} angular distribution emission is shown in Fig. 3(c). Finally, we have confirmed that for a given spectral emission region, similar interference patterns with similar angular spacing are obtained for any excitation position along the same single plasmonic chain (Fig. 3(d)). The results are also reproducible for different chains with the same parameters.

The images of the Nd^{3+} emitted light in the real space in the presence and in the absence of plasmonic chain, together with the corresponding profiles along the maximum PL intensity are shown in Fig. 4(a) and Fig. 4(b), respectively. They clearly show the increase of the PL intensity

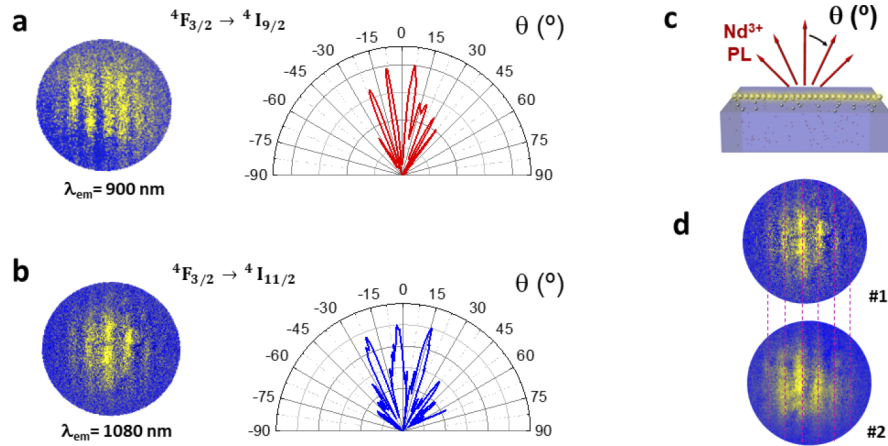


Fig. 3. Fringe patterns and azimuthal polar plots for two different Nd^{3+} emission transitions: (a) at 900 nm and (b) at 1080 nm. (c) Sketch of the directional emission displayed by Nd^{3+} emitters located in the proximities of the metallic chain. (d) Interference patterns obtained at 1080 nm for two different excitation positions along the same plasmonic chain; the dashed lines show the similar angular spacing obtained and the reproducibility of the results.

in the vicinities of the chain, in agreement with the plasmonic enhancement of the involved field radiation due to the strong local confinement [37]. Since the excitation region extends beyond the plasmonic chain (see Fig. 1(a)), the emission images contain a major contribution from Nd^{3+} ions not coupled to the chain. The real space image contains both the coherent and the incoherent emission without any angular selection. Therefore, contrary to the images obtained in the Fourier space, a uniform emission pattern is obtained in the real space, since the experimental conditions used in our work (fluorescence microscopy) do not allow to spatially resolve the emission produced by the minority of the excited Nd^{3+} ions coupled to the chain.

Fluorescence lifetime measurements were carried out to compare the Nd^{3+} emission dynamics from the bare region with that from the vicinities of the plasmonic chain. Figure 4(c) shows the Nd^{3+} temporal decays obtained in both cases. In the absence of plasmonic chain, a single exponential decay time of around 100 μs was measured in agreement with the reported fluorescence decay time of $\text{Nd}^{3+}:\text{LiNbO}_3$ at room temperature [43]. On the other hand, a systematic and reproducible decay time shortening is observed in the vicinities of the plasmonic chain. This lifetime reduction can be interpreted as an additional indication of the spatial coherence due to the coupling between the Nd^{3+} ions and the plasmonic chain, which could lead to an increase of the spontaneous emission rate. Note that the enhancement of the PL intensity in the presence of the plasmonic chain (Fig. 4(b)) allows to disregard the decay time reduction as a result of a fluorescence quenching. In fact, the emission decay analysis at the immediacy of the plasmonic chain reveals the contribution of an additional faster component with a lifetime value of about half of that obtained from the bare system. However, its precise value could not be determined, among others, due to the presence of the above mentioned emission background from the non-coupled ions unaffected by the plasmonic chain.

To corroborate numerically the effect of the plasmonic chain on the Nd^{3+} emission pattern and understand the physical origin of the experimentally measured directional emission we have employed a commercial-grade simulator (*Lumerical Solutions Inc.*) based on the finite-difference time-domain (FDTD) method [44]. See Methods section for details on the numerical approach. In the simulations, the plasmonic chain was placed along the x -axis on top of a semi-infinite substrate with the refractive index of LiNbO_3 ($n = 2.2$ @ 900 nm) [45]. Single Nd^{3+} ions,

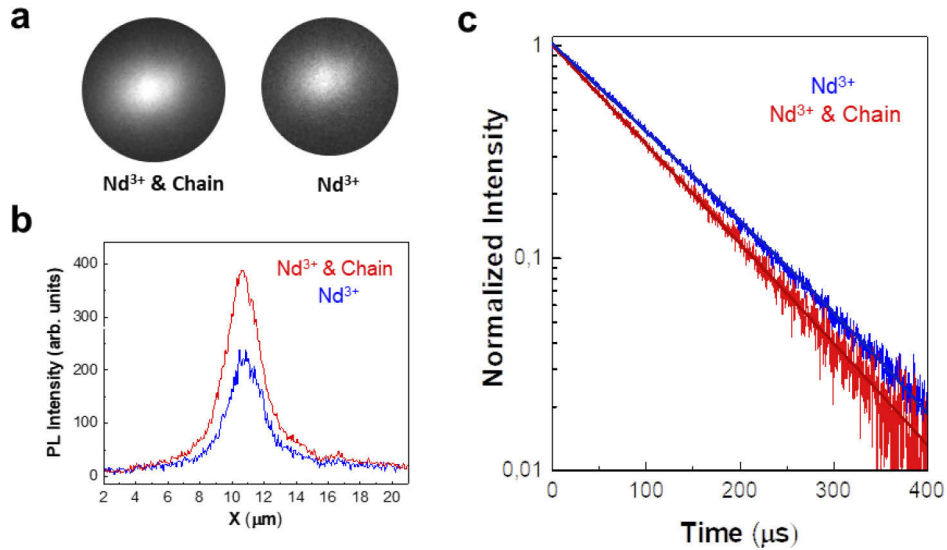


Fig. 4. (a) Nd^{3+} PL images in the real space at 900 nm obtained in the vicinity of the plasmonic chain (left) and in the absence of the plasmonic chain (right). (b) Spatial intensity profile of the Nd^{3+} PL in the presence (red line) and in the absence of plasmonic chain (blue line). (c) Decay curves of Nd^{3+} emission in the absence of the plasmonic chain (blue) and in the vicinities of the plasmonic chain (red). The results correspond to the de-excitation from the $^4\text{F}_{3/2}$ metastable level.

embedded into the semi-infinite substrate in the proximities of the Ag NP chain (at $z = -3$ nm, with $z = 0$ nm defining the interface between air and LiNbO_3), were simulated by single dipole sources oscillating at $\lambda = 900$ nm and oriented parallel to the plasmonic chain, since the antenna effect is most prominent for this particular orientation.

As starting point, to describe the hybrid system, Fig. 5(a) shows the simulated near field of the system in the x - z plane (cross section along the chain) obtained under the illumination of a single dipole source (Nd^{3+} ion) located at $x = 0$ nm. The representation corresponds to the electric field amplitude of the system in the presence of the plasmonic chain, normalized to the electric field amplitude of the same system in the absence of the plasmonic chain, i.e., $|E_{\text{NP}}|/|E_{\text{BARE}}|$. A plasmon mode with high intensity lobes both within the substrate and in the upper far field emission region is clearly identified. The plasmonic mode exhibits very low losses due to the almost negligible penetration of the electric field in the Ag NPs and in agreement with previous results [41]. The corresponding projection to the far field is shown in Fig. 5(b) and it does not display any specific directional pattern. To confirm the lateral field confinement produced by the chain, Fig. 5(c) shows a detail of the field amplitude distribution produced by the dipole in the presence of the plasmonic chain for two transverse planes located at 25 nm (mid-plane of the chain) and 55 nm above the surface. These field distributions are compared to those obtained at the same transverse planes for a plane wave polarized along the chain axis (see Fig. 5(d)). In both cases (dipole or plane wave excitation) the lateral field confinement produced by the metallic chain is clearly observed.

Next, to investigate the collective emission from several emitters in the vicinity of the chain, we considered five quantum emitters, again oriented along the chain axis to maximize the interaction with the plasmon mode. Due to computational limitations, we cannot consider a larger number of dipoles, but we expect our model can capture the main physical ingredients of the problem. In the simulations, a single dipole was located at $x = 0$ nm, and four additional equidistant dipoles were

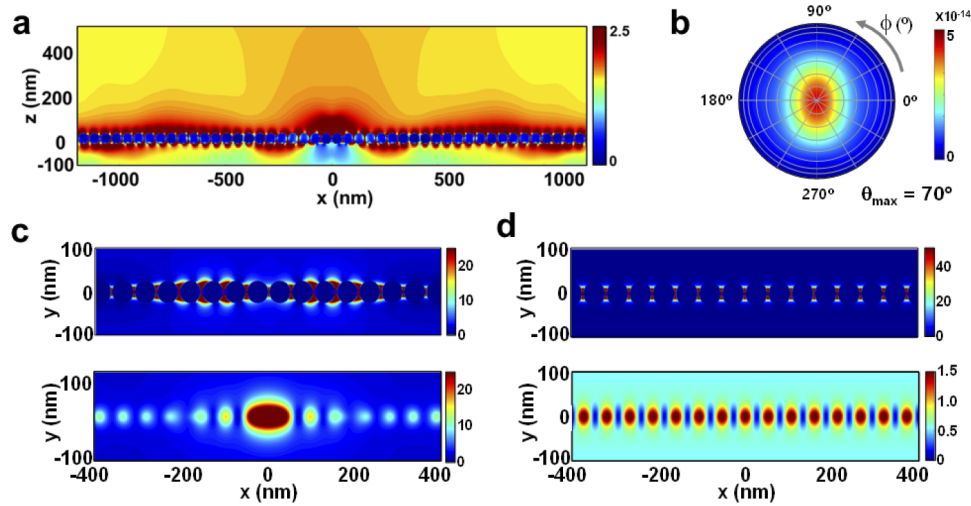


Fig. 5. (a) Calculated electric field amplitude response in the x - z plane of a horizontally oriented electric dipole at $\lambda = 900$ nm in the LiNbO_3 substrate located at $x = 0$ and $z = -3$ nm in the presence of a plasmonic NP chain. The representation is normalized to the electric field amplitude in the absence of plasmonic chain, *i.e.*, $|E_{\text{NP}}|/|E_{\text{BARE}}|$. (b) Simulated far field 2D angular projection. Concentric grey circles indicate θ angles increasing in steps of 10° . (c) Detail of the field amplitude distribution in transversal planes at 25 nm (top) and 55 nm (bottom) above the LiNbO_3 surface of (c) a horizontal oriented electric dipole in the presence of the plasmonic chain and (d) a plane wave with the electric field oscillating parallel to the chain axis.

placed symmetrically at $x = \pm 500$ nm and 1000 nm (Fig. 6). The selected distances correspond to representative cases that serve us to attain qualitative physical insight into the process here taking place. To identify the possibility of having plasmon-mediated interaction between the emitters, we carried out simulations corresponding to two different physical scenarios. In the first one, the dipoles oscillate coherently in the absence of the plasmonic chain (by setting their phases equal). The second one considers the physical situation in which the interaction of the Nd^{3+} emitters is plasmon-assisted. In this case, a two-step calculation was performed: in the first place, the phase of the electric field component parallel to the chain axis in the x - z plane of a single dipole source ($\varphi_{E_x}(x, z)$) placed at $x = 0$ nm was computed (see Supplement 1, Fig. S1); subsequently, the phases of each of the five quantum emitters were imposed to be those of the plasmon mode according to their spatial position and to results in Supplement 1, Fig. S1, *i.e.*, $\varphi_{E_x}(x, z)$ values were assigned to each dipole based on their spatial location. By doing so, the phase of the five dipole sources is enforced to match that of the plasmon mode emulating a plasmon-mediated interaction. Figure 6(a) shows the results obtained in the first scenario, when the five dipoles oscillate in phase in the absence of plasmonic chain. Although in the near-field, a certain tendency of fringe formation is observed, it is very weakly discerned in the far field projection. However, when the emitters oscillate in phase with the chain plasmon mode (Fig. 6(b)), a stronger contrast in the near-field at the vicinities of the dipoles is obtained, and the far field projection displays clear directional emission features and fringes qualitatively consistent with those experimentally observed. Since the coupling strength of the emitters to the collective mode and the out-coupling to far field radiation depends, amongst others, upon the emitters efficiency and their location with respect to the plasmonic NP chain [46], it is expected that the different Nd^{3+} ions located at different positions in the proximities of the chain will contribute differently to the far field. Complementary results on the effect of the number of emitters and

their spatial location in the electric near field and far field projection have been analyzed. In [Supplement 1](#), Figs. S2 and S3 show results for three emitters and the evolution of the far field patterns generated for different separation distances between them. Results for five dipole sources located at not equidistant positions are displayed in [Supplement 1](#), Fig. S4. Although in our simulations we cannot include additional dipole sources due to computational limitations, it is expected that the contribution of added dipole sources enlarges the number of fringes to some extent, according to the experimental angles. A statistical estimation of the overall efficiency of the studied process, including the quantum-emitter plasmonic mode coupling process as well as the out-coupling to far field radiation, will require carrying out a statistically-relevant number of FDTD simulations describing the response of the system to different locations and orientations of the quantum emitters. Although such analysis is beyond our computational capabilities, the good agreement found between the numerical and experimental far-field emission profiles makes us confident that the provided description captures the main ingredients of the studied problem.

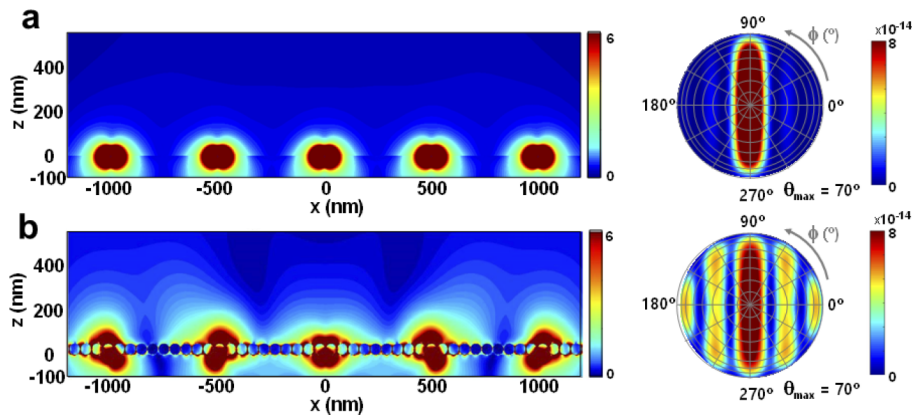


Fig. 6. Electric field amplitude in the x - z plane generated by five horizontally oriented electric dipoles oscillating at 900 nm. The dipoles are placed into the LiNbO_3 substrate at $z = -3$ nm, and symmetrically placed along the chain axis at $x = 0$ nm, $x = \pm 500$ nm, and $x = \pm 1000$ nm. The corresponding simulated far field 2D angular projection is shown on the right side. Concentric grey circles indicate θ angles, increasing in steps of 10° . (a) The five horizontally oriented electric dipoles oscillate in phase in the absence of the plasmonic chain ($\varphi_{E_x}(x, z) = 0$). (b) The five dipoles are forced to oscillate in phase with the plasmon mode by setting their phases $\varphi_{E_x}(x, z)$ according to their spatial position and based on calculations shown in [Supplement 1](#), Fig. S1.

The results derived from the experiments and simulations show the capability of a linear chain of interacting Ag NPs to control the emission of Nd^{3+} ions, inducing their oscillation with the phase relationship imposed by the chain plasmon mode in the absence of optical cavity. The observed directional emission is the result of the spatial coherence emerging from the coupling of the dipole sources to the plasmon excitation along the chain, which transforms the spontaneous emission from the incoherent Nd^{3+} ions into spatially coherent light. Light coupled out from the system interferes constructively in defined directions, yielding specific directional emission. Finally, it is worth mentioning the emission lifetime reduction of those Nd^{3+} ions coupled to the chain. In this respect, superradiance mediated by nanostructures [23,47] cannot be disregarded.

3. Summary and conclusions

In conclusion, the near-field coherent coupling of the emitting RE ions with the plasmon chain mode evidences the plasmon mediated long distance ion-ion interaction processes as responsible

for the spatial coherence between the RE emitters. The capability of inducing coherence and directionality in the emission of RE ions by a single plasmonic chain could be exploited in highly integrated systems for wavelength multiplexing and optical signal processing in nanocircuits. Furthermore, the possibility of fabricating ultra-long linear chains (millimeter length) along with the robustness and low dissipative losses displayed by the longitudinal mode supported by the plasmonic chain, allows room temperature spatial coherence in solid-state platforms, which hold promise for scalable quantum light-matter interfaces and photonic networks. The results can be extended to the rich variety of optical transitions provided by the RE emitters, which would expand the control to different spectral ranges with the subsequent tunability in the angular distribution and enhancement factors in the absence of optical cavity.

4. Materials and methods

4.1. Sample preparation

Nd^{3+} doped periodically poled LiNbO_3 was grown by off-centered Czochralski technique by adding Nd^{3+} in the form of Nd_2O_3 in the melt [48]. Rotation and pulling rates employed (30 rpm and 1mm/h, respectively) produced alternate domain structures with periodicity 3 μm . Z-cut plates samples (0.1 \times 1 \times 1 cm) were cut and polished to optical quality.

Chains of Ag NPs were photodeposited by illuminating the surface of the $\text{Nd}^{3+}:\text{LiNbO}_3$ crystal with a UV lamp with its main line at 253.6 nm (mercury pen lamp UVP model 11SC), while the sample was immersed in a 0.01 M AgNO_3 solution at 50 °C. The emission power of the UV lamp was 5400 μWcm^{-2} at a distance of 1.9 cm and the illumination time was 10 min. More details on the sample preparation can be found elsewhere [42].

4.2. Optical measurements

Fourier microscopy experiments were carried out exciting the sample at 590 nm with a CW OPSSL laser (Coherent Genesis MX) by using a 100x (0.9NA) Olympus microscope objective, which was also used to collect the emission in backscattering configuration. To image the back focal plane of the objective lens a tube lens was used to form an image at the native image plane (IP). A converging lens ($f = 125$ mm) placed at a focal distance from the IP transformed this native image to its back focal plane where a sCMOS camera (Andor Zyla 4.2) was located. Band pass filters were placed before the camera to select the different Nd^{3+} emission transitions.

Fluorescence decay time experiments were carried out by a confocal microscope. A 100x objective was used to focus the excitation on the $\text{Nd}^{3+}:\text{LiNbO}_3$ surface. For the excitation, the laser beam was set at 590 nm. The emission was collected in backscattered geometry with the same objective lens and directed by an optical fiber to a Peltier cooled photomultiplier tube connected to a digital oscilloscope.

4.3. Numerical simulations

A commercial-grade simulator based on the finite-difference time-domain (FDTD) method is used to calculate the electromagnetic fields in the system. In the 3-dimensional (3D) simulations, a chain of 50 spherical Ag NPs of 50 nm size with a gap distance between two particles of 2 nm is considered. The plasmonic chain of Ag NPs is placed along the x -direction, at $z = 0$ nm, and on top of a semi-infinite substrate with refractive index 2.2, resembling that of the LiNbO_3 bulk material [45]. The dispersion of the metal is fitted using a Drude model. Perfectly matched layer (PML) absorbing boundary conditions (specifically, the stretched coordinate PML type) are applied along the x , y and z directions, and a refined mesh below 1 nm is taken in a volume spanning around the Ag NPs chain until converged results are attained. The emission of Nd^{3+} ions at $\lambda = 900$ nm is represented by single dipole sources embedded into the semi-infinite substrate 3 nm below the Ag NP chain, i.e., at $z = -3$ nm. Due to computational reasons, and to

obtain converged results, the single dipole sources illuminating the system are set at the same time at different x positions along the chain axis.

Funding. Agencia Estatal de Investigación (CEX2018-000805-M, MAT2016-76106-R, PID2019-108257GB-I00, RTI2018-098452-B-I00); Comunidad de Madrid (S11/PJI/2019-00105); Nederlandse Organisatie voor Wetenschappelijk Onderzoek (Vici Project No. 680-47-628).

Disclosures. The authors declare no conflicts of interest.

Data availability. Data underlying the results presented in this paper are not publicly available at this time but may be obtained from the authors upon reasonable request.

Supplemental document. See [Supplement 1](#) for supporting content.

References

1. M. H. Fang, J. L. Leañó, and R. S. Liu, "Control of Narrow-Band Emission in Phosphor Materials for Application in Light-Emitting Diodes," *ACS Energy Lett.* **3**(10), 2573–2586 (2018).
2. G. J. Hoerder, M. Seibald, D. Baumann, T. Schröder, S. Peschke, P. C. Schmid, T. Tyborski, P. Pust, I. Stoll, M. Bergler, C. Patzig, S. Reißaus, M. Krause, L. Berthold, T. Höche, D. Johrendt, and H. Huppertz, "Sr[Li₂Al₂O₂N₂]:Eu²⁺ - A high performance red phosphor to brighten the future," *Nat. Commun.* **10**(1), 1824 (2019).
3. F. E. Schubert and J. K. Kim, "Solid-State Light Sources Getting Smart," *Science* **308**(5726), 1274–1278 (2005).
4. J. C. G. Bünzli and S. V. Eliseeva, "Lanthanide NIR luminescence for telecommunications, bioanalyses and solar energy conversion," *J. Rare Earths* **28**(6), 824–842 (2010).
5. Y. Liu, Y. Lu, X. Yang, X. Zheng, S. Wen, F. Wang, X. Vidal, J. Zhao, D. Liu, Z. Zhou, C. Ma, J. Zhou, J. A. Piper, P. Xi, and D. Jin, "Amplified stimulated emission in upconversion nanoparticles for super-resolution nanoscopy," *Nature* **543**(7644), 229–233 (2017).
6. S. Wilhelm, "Perspectives for Upconverting Nanoparticles," *ACS Nano* **11**(11), 10644–10653 (2017).
7. Y. Lu, J. Zhao, R. Zhang, Y. Liu, D. Liu, E. M. Goldys, X. Yang, P. Xi, A. Sunna, J. Lu, Y. Shi, R. C. Leif, Y. Huo, J. Shen, J. A. Piper, J. P. Robinson, and D. Jin, "Tunable lifetime multiplexing using luminescent nanocrystals," *Nat. Photonics* **8**(1), 32–36 (2014).
8. S. H. Nam, Y. M. Bae, Y. I. Park, J. H. Kim, H. M. Kim, J. S. Choi, K. T. Lee, T. Hyeon, and Y. D. Suh, "Long-Term Real-Time Tracking of Lanthanide Ion Doped Upconverting Nanoparticles in Living Cells," *Angew. Chem. Int. Ed.* **50**(27), 6093–6097 (2011).
9. J. C. G. Bünzli, "Lanthanide Luminescence for Biomedical Analyses and Imaging," *Chem. Rev.* **110**(5), 2729–2755 (2010).
10. X. Huang, S. Han, W. Huang, and X. Liu, "Enhancing solar cell efficiency: the search for luminescent materials as spectral converters," *Chem. Soc. Rev.* **42**(1), 173–201 (2013).
11. S. V. Eliseeva and J. C. G. Bünzli, "Lanthanide luminescence for functional materials and bio-sciences," *Chem. Soc. Rev.* **39**(1), 189–227 (2010).
12. Z. Qu, J. Shen, Q. Li, F. Xu, F. Wang, X. Zhang, and C. Fan, "Near-IR emissive rare-earth nanoparticles for guided surgery," *Theranostics* **10**(6), 2631–2644 (2020).
13. J. M. Kindem, A. Ruskuc, J. G. Bartholomew, J. Rochman, Y. Q. Huan, and A. Faraon, "Control and single-shot readout of an ion embedded in a nanophotonic cavity," *Nature* **580**(7802), 201–204 (2020).
14. R. Kolesov and J. Wrachtrup, "A rare quantum leap," *Nat. Phys.* **16**(5), 503–504 (2020).
15. D. Serrano, J. Karlsson, A. Fossati, A. Ferrier, and P. Goldner, "All-optical control of long-lived nuclear spins in rare-earth doped nanoparticles," *Nat. Commun.* **9**(1), 2127 (2018).
16. T. Zhong, J. M. Kindem, J. G. Bartholomew, J. Rochman, I. Craiciu, E. Miyazono, M. Bettinelli, E. Cavalli, V. Verma, S. W. Nam, F. Marsili, M. D. Shaw, A. D. Beyer, and A. Faraon, "Nanophotonic rare-earth quantum memory with optically controlled retrieval," *Science* **357**(6358), 1392–1395 (2017).
17. T. Zhong, J. M. Kindem, E. Miyazono, and A. Faraon, "Nanophotonic coherent light–matter interfaces based on rare-earth-doped crystals," *Nat. Commun.* **6**(1), 8206 (2015).
18. P. Molina, E. Yraola, M. O. Ramírez, C. Tserkezis, J. L. Plaza, J. Aizpurua, J. Bravo-Abad, and L. E. Bausa, "Plasmon-Assisted Nd³⁺-Based Solid-State Nanolaser," *Nano Lett.* **16**(2), 895–899 (2016).
19. D. Hernandez-Pinilla, P. Molina, C. de las Heras, J. Bravo-Abad, L. E. Bausa, and M. O. Ramírez, "Multiline Operation from a Single Plasmon-Assisted Laser," *ACS Photonics* **5**(2), 406–412 (2018).
20. A. Fernandez-Bravo, D. Wang, E. S. Barnard, A. Teitelboim, C. Tajon, J. Guan, G. C. Schatz, B. E. Cohen, E. M. Chan, P. J. Schuck, and T. W. Odom, "Ultralow-threshold, continuous-wave upconverting lasing from subwavelength plasmons," *Nat. Mater.* **18**(11), 1172–1176 (2019).
21. D. Hernández-Pinilla, J. Cuerda, P. Molina, M. O. Ramírez, and L. E. Bausa, "Spectral Narrowing in a Subwavelength Solid-State Laser," *ACS Photonics* **6**(9), 2327–2334 (2019).
22. L. Sanchez-Garcia, M. O. Ramírez, R. M. Sole, J. J. Carvajal, F. Diaz, and L. E. Bausa, "Plasmon-induced dual-wavelength operation in a Yb³⁺ laser," *Light: Sci. Appl.* **8**(1), 14 (2019).
23. D. Martín-Cano, L. Martín-Moreno, F. J. García-Vida, and E. Moreno, "Resonance Energy Transfer and Superradiance Mediated by Plasmonic Nanowaveguides," *Nano Lett.* **10**(8), 3129–3134 (2010).

24. H. Varguet, S. Guérin, H. Jauslin, and G. Colas des Francs, "Cooperative emission in quantum plasmonic superradiance," *Phys. Rev. B* **100**(4), 041115 (2019).
25. N. Kuzmin, G. W. 't Hooft, E. R. Eliel, G. Gbur, H. F. Schouten, and T. D. Visser, "Enhancement of spatial coherence by surface plasmons," *Opt. Lett.* **32**(5), 445–447 (2007).
26. D. Li and D. Pacifici, "Strong amplitude and phase modulation of optical spatial coherence with surface plasmon polaritons," *Sci. Adv.* **3**(10), e1700133 (2017).
27. Y. Osaka, N. Yokoshi, and H. Ishihara, "Radiation-Induced Correlation between Molecules Nearby Metallic Antenna Array," *Int. J. Antennas Propag.* **2015**, 1–6 (2015).
28. G. Vecchi, V. Giannini, and J. G. Rivas, "Shaping the Fluorescent Emission by Lattice Resonances in Plasmonic Crystals of Nanoantennas," *Phys. Rev. Lett.* **102**(14), 146807 (2009).
29. S. Viarbitskaya, O. Demichel, B. Cluzel, G. Colas des Francs, and A. Bouhelier, "Delocalization of Nonlinear Optical Responses in Plasmonic Nanoantennas," *Phys. Rev. Lett.* **115**(19), 197401 (2015).
30. T. B. Hoang, G. M. Akselrod, A. Yang, T. W. Odom, and M. H. Mikkelsen, "Millimeter-Scale Spatial Coherence from a Plasmon Laser," *Nano Lett.* **17**(11), 6690–6695 (2017).
31. L. Shi, X. Yuan, Y. Zhang, T. Hakala, S. Yin, D. Han, X. Zhu, B. Zhang, X. Liu, P. Törmä, W. Lu, and J. Zi, "Coherent fluorescence emission by using hybrid photonic–plasmonic crystals," *Laser Photonics Rev.* **8**(5), 717–725 (2014).
32. G. Lozano, G. Grzela, M. A. Verschuuren, M. Ramezani, and J. G. Rivas, "Tailor-made directional emission in nanoimprinted plasmonic-based light-emitting devices," *Nanoscale* **6**(15), 9223–9229 (2014).
33. M. Ramezani, A. Halpin, A. I. Fernandez, J. Feist, S. R. K. Rodriguez, F. J. Garcia-Vidal, and J. Gómez Rivas, "Plasmon-exciton-polariton lasing," *Optica* **4**(1), 31–37 (2017).
34. S. Aberra Guebrou, C. Symonds, E. Homeyer, J. C. Plenat, Y. N. Gartstein, V. M. Agranovich, and J. Bellessa, "Coherent Emission from a Disordered Organic Semiconductor Induced by Strong Coupling with Surface Plasmons," *Phys. Rev. Lett.* **108**(6), 066401 (2012).
35. L. Shi, T. K. Hakala, H. T. Rekola, J. P. Martikainen, R. J. Moerland, and P. Törmä, "Spatial Coherence Properties of Organic Molecules Coupled to Plasmonic Surface Lattice Resonances in the Weak and Strong Coupling Regimes," *Phys. Rev. Lett.* **112**(15), 153002 (2014).
36. S. Murai, M. Verschuuren, G. Lozano, G. Pirruccio, S. Rodriguez, and J. G. Rivas, "Hybrid plasmonic-photonic modes in diffractive arrays of nanoparticles coupled to light-emitting optical waveguides," *Opt. Express* **21**(4), 4250–4262 (2013).
37. E. Yraola, P. Molina, J. L. Plaza, M. O. Ramírez, and L. E. Bausa, "Spontaneous Emission and Nonlinear Response Enhancement by Silver Nanoparticles in a Nd³⁺-Doped Periodically Poled LiNbO₃ Laser Crystal," *Adv. Mater* **25**(6), 910–915 (2013).
38. P. Molina, M. O. Ramírez, J. García Solé, L. E. Bausá B, and J. García, "Selective rearrangement of Nd³⁺ centers in LiNbO₃ under ferroelectric domain inversion by electron beam writing," *Phys. Rev. B* **78**(1), 014114 (2008).
39. F. J. García de Abajo and J. Aizpurua, "Numerical simulation of electron energy loss near inhomogeneous dielectrics," *Phys. Rev. B* **56**(24), 15873–15884 (1997).
40. E. Yraola, L. Sánchez-García, C. Tserkezis, P. Molina, M. O. Ramírez, J. Aizpurua, and L. E. Bausá, "Polarization-selective enhancement of Nd³⁺ photoluminescence assisted by linear chains of silver nanoparticles," *J. Lumin.* **169**, 569–573 (2016).
41. M. O. Ramírez, P. Molina, A. Gómez-Tornero, D. Hernández-Pinilla, L. Sánchez-García, S. Carretero-Palacios, and L. E. Bausá, "Hybrid Plasmonic–Ferroelectric Architectures for Lasing and SHG Processes at the Nanoscale," *Adv. Mater* **31**(35), 1901428 (2019).
42. P. Molina, E. Yraola, M. O. Ramírez, J. L. Plaza, C. de las Heras, and L. E. Bausá, "Selective Plasmon Enhancement of the 1.08 μm Nd³⁺ Laser Stark Transition by Tailoring Ag Nanoparticles Chains on a PPLN Y-cut," *Nano Lett.* **13**(10), 4931–4936 (2013).
43. T. Y. Fan, A. Cordova-Plaza, M. J. F. Digonnet, R. L. Byer, and H. J. Shaw, "Nd:MgO:LiNbO₃ spectroscopy and laser devices," *J. Opt. Soc. Am. B* **3**(1), 140–148 (1986).
44. Lumerical Inc. <https://www.lumerical.com/products/>.
45. D. E. Zelmon, D. L. Small, and D. Jundt, "Infrared corrected Sellmeier coefficients for congruently grown lithium niobate and 5 mol. % magnesium oxide-doped lithium niobate," *J. Opt. Soc. Am. B* **14**(12), 3319–3322 (1997).
46. H. Aouani, O. Mahboub, E. Devaux, H. Rigneault, T. W. Ebbesen, and J. Wenger, "Plasmonic Antennas for Directional Sorting of Fluorescence Emission," *Nano Lett.* **11**(6), 2400–2406 (2011).
47. P. Solano, P. Barberis-Blostein, F. K. Fatemi, L. A. Orozco, and S. L. Roslton, "Super-radiance reveals infinite-range dipole interactions through a nanofiber," *Nat. Commun.* **8**(1), 1857 (2017).
48. V. Bermudez, M. D. Serrano, and E. Dieguez, "Bulk periodic poled lithium niobate crystals doped with Er and Yb," *J. Cryst. Growth* **200**(1–2), 185–190 (1999).